# Water Oxidation on Pure and Doped Hematite (0001) Surfaces: Prediction of Co and Ni as Effective Dopants for Electrocatalysis

Peilin Liao,[†] John A. Keith,[‡] and Emily A. Carter*[,‡,§]

Departments of [†]Chemistry and [‡]Mechanical and Aerospace Engineering, and [§]Program in Applied and Computational Mathematics and Gerhard R. Andlinger Center for Energy and the Environment, Princeton University, Princeton, New Jersey 08544-5263, United States

S *Supporting Information*

ABSTRACT: In photoelectrochemical cells, sunlight may be converted into chemical energy by splitting water into hydrogen and oxygen molecules. Hematite (α-Fe_2O_3) is a promising photoanode material for the water oxidation component of this process. Numerous research groups have attempted to improve hematite's photocatalytic efficiency despite a lack of foundational knowledge regarding its surface reaction kinetics. To elucidate detailed reaction mechanisms and energetics, we performed periodic density functional theory + U calculations for the water oxidation reaction on the fully hydroxylated hematite (0001) surface. We investigate two different concentrations of surface reactive sites. Our best model involves calculating water oxidation mechanisms on a pure (1×1) hydroxylated hematite slab (corresponding to 1/3 ML of reactive sites) with an additional overlayer of water molecules to model solvation effects. This yields an overpotential of 0.77 V, a value only slightly above the 0.5−0.6 V experimental range. To explore whether doped hematite can exhibit an even lower overpotential, we consider cation doping by substitution of Fe by Ti, Mn, Co, Ni, or Si and F anion doping by replacing O on the fully hydroxylated surface. The reaction energetics on pure or doped hematite surfaces are described using a volcano plot. The relative stabilities of holes on the active O anions are identified as the underlying cause for trends in energetics predicted for different dopants. We show that moderately charged O anions give rise to smaller overpotentials. Co- or Ni-doped hematite surfaces give the most thermodynamically favored reaction pathway (lowest minimum overpotential) among all dopants considered. Very recent measurements (*Electrochim. Acta* **2012**, *59*, 121−127) reported improved reactivity with Ni doping, further validating our predictions.
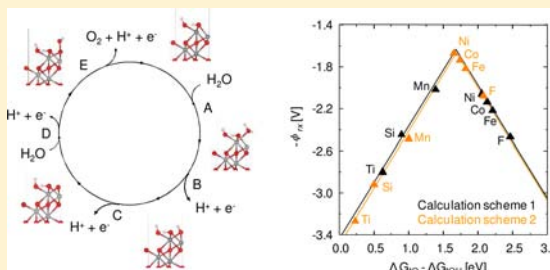
1. INTRODUCTION

Solar energy is a promising resource to help satisfy a fast-growing global energy demand. Photoelectrochemical reactions can harvest solar energy by using sunlight to provide energy for endoergic chemical reactions, which in turn create reaction products that store chemical energy. The water splitting reaction, $H_2O \rightarrow H_2 + O_2$ ($E^0 = -1.23$ V), produces H_2 energy carriers,[1] which can be used as a fuel itself or as a feedstock to produce liquid fuels. Water splitting requires not only energy input but also photoelectrocatalysts to accelerate the reaction. Hematite (α-Fe_2O_3, "α-" is omitted henceforth) has shown promise as a photocatalytic anode material. It has an indirect optical band gap of 1.9−2.2 eV,[2,3] which can absorb approximately 40% of the solar spectrum. It is cheap, abundant, nontoxic, and stable against corrosion. Its valence band and conduction band alignments permit water oxidation to produce oxygen, but it cannot form hydrogen without an applied voltage.[1] Recently, Ti-doped hematite surfaces modified by exposure to a CoF_3 solution were shown to shift the conduction band position so that an external bias is not required to generate hydrogen from water.[4] This offers the promise of full water splitting (as opposed to just oxidation). Hematite has some major shortcomings, however, including

low conductivity, a small optical absorption coefficient, and fast electron−hole recombination rates. Consequently, improving the efficiency of hematite as a photoanode is an active area of research.[5,6] N-type doping with Ti, Si, Ge, Zr, etc., increases carrier concentrations and hence conductivity.[7−10] Nanostructuring shortens hole diffusion pathways and thereby reduces electron−hole recombination.[11−15] Surface modifications with cocatalysts[16−18] or by doping[12,19−21] improve reaction kinetics and reduce overpotentials. By incorporating these strategies, a water oxidation photocurrent of >3 mA/cm^2 was achieved using nanostructured hematite with an IrO_2 cocatalyst at an applied potential of +1.23 V versus the reversible hydrogen electrode under standard solar illumination conditions.[17]

Hematite has a corundum lattice structure, with lattice constants $a = 5.035$ Å and $c = 13.747$ Å.[22] Below the Néel temperature ($T_N = 963$ K), Fe_2O_3 is antiferromagnetic with weak ferromagnetism.[23] The high-spin d^5 Fe^{3+} cations within one bilayer in the (0001) planes are ferromagnetically coupled to each other while antiferromagnetically coupled to the

adjacent Fe bilayers. The two natural growth faces of hematite are the (0001) and the (01$\bar{1}$2) surfaces.[24] Experimentally, both surfaces have been characterized under ultrahigh vacuum (UHV)[25−30] and when in contact with water.[31−34] Theoretically, the surface energies of the two surfaces under vacuum are similar—the (0001) surface is ∼0.1 J/m^2 less stable.[35] Here we examine the water oxidation reaction on the (0001) surface as a first step toward understanding the redox surface chemistry of hematite. The termination of the (0001) surface is less complicated with fewer reconstructions than other surfaces. We expect that the insights gleaned from the current study on the (0001) surface will also shed light on related surface chemistry on the hematite (01$\bar{1}$2) surface.

Under UHV conditions, the single-layer Fe-terminated (0001) surface, which is stoichiometric and nonpolar, has been suggested to be the most stable by X-ray photoelectron diffraction and scanning tunneling microscopy (STM) experiments.[27,29] Coexistence of the single-layer Fe-terminated surface and the O-terminated surface was observed by STM and low-energy electron diffraction (LEED) under an oxygen pressure of $10^{-4}-10^{-1}$ mbar. This coexistence was also predicted for certain oxygen partial pressures by full-potential linearized augmented plane wave density functional theory (DFT) calculations within the generalized gradient approximation (GGA) for exchange-correlation (XC).[26,28,36] DFT-GGA calculations using projector augmented wave (PAW) potentials predicted that at a constant oxygen partial pressure of 0.2 bar, the most stable Fe$_2$O$_3$ (0001) surface below 500 K is the O-terminated surface.[37] Because self-interaction errors (SIEs) inherent in standard Kohn−Sham DFT[38] are large for localized Fe 3d electrons in Fe$_2$O$_3$, standard DFT incorrectly predicts narrow band gaps for bulk hematite[39,40] and overestimates the interlayer spacings in both hematite bulk[40] and surface[35] structures. The DFT+U method,[41] which includes exact intra-atomic exchange energy, has been proposed and successfully applied to strongly correlated materials to correct for the SIEs.[42] Therefore, the above conclusions derived from DFT calculations may change if the more physically correct DFT+U theory is employed, as done here.

Water adsorption on the Fe$_2$O$_3$ (0001) surface has been experimentally characterized with various surface science techniques.[31,34,43−48] In one study using X-ray photoelectron spectroscopy (XPS), ultraviolet photoelectron spectroscopy, Auger, and temperature-programmed desorption,[43] only ice condensation was observed on the stoichiometric surface at 175−220 K, while sputtered surfaces containing oxygen vacancies and concomitantly reduced Fe^{2+} ions chemisorb water strongly. Another study (on hydrated and hydroxylated hematite (0001) surfaces using XPS, scanning force microscopy, scanning electron microscopy, X-ray diffraction, and LEED)[46] found adsorption and dissociation of H$_2$O were restricted to the top monolayer (ML) of the surfaces under ambient conditions. The most recent study using XPS for water adsorption on hematite (0001) near ambient conditions observed hydroxylation of only the topmost surface layer before water molecule adsorption.[34] Trainor et al.[31] studied the hydrated hematite (0001) surface at room temperature with a nearly water-saturated He atmosphere using crystal truncation rod (CTR) diffraction and DFT-GGA calculations. Spacings of the terminating Fe and O layers were measured by CTR. Identifications of the terminations were made by comparing the measured spacings to those predicted by DFT and taking into account the thermodynamic stabilities of different terminations
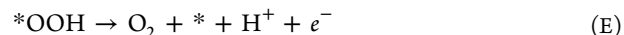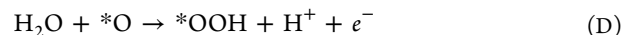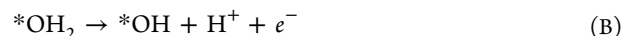
predicted by DFT. That study suggested two different hydroxylated domains coexist: one domain corresponds to a full hydroxylation of the single-layer Fe-terminated surface ((HO)$_3$-Fe-(HO)$_3$-Fe-R, where "R" represents the remaining layers in the bulk), and another domain is a fully hydroxylated O-terminated surface ((HO)$_3$-Fe-Fe-R) resulting from removal of a Fe(OH)$_3$ species from the first structure. Since DFT-GGA overestimates the spacings of hematite as already discussed above, the identifications based on comparing experimental data to DFT-GGA values should be viewed with caution.

Theoretically, water adsorption and hydroxylation of hematite surfaces have been studied by both atomistic simulations[49,50] and DFT.[51,52] According to one classical potential simulation,[50] the structure with Fe(OH)$_3$ dissociating from the surface was 0.82 J/m^2 more stable than the structure with Fe(OH)$_3$ attached to the surface, implying desorption of Fe(OH)$_3$. DFT-GGA studies of Fe-terminated or defective hematite (0001) surfaces predicted that defective surfaces with Fe adatoms or vacancies are more reactive toward H$_2$O.[51,52] To our knowledge, theoretical studies detailing water oxidation mechanisms on hematite (0001) surfaces are not available.

Since the (HO)$_3$-Fe-(HO)$_3$-Fe-R domains might gradually evolve to (HO)$_3$-Fe-Fe-R after Fe(OH)$_3$ dissociates, here we study surface chemistry of the hematite (0001) surface with the (HO)$_3$-Fe-Fe-R model termination. We also investigate doping effects on the surface chemistry. For cation substitutions, several first-row transition metals (Ti, Mn, Co, and Ni) are considered. These first-row transition metal cations have similar ionic radii to Fe, but they have different numbers of 3d electrons, giving rise to different stable oxidation states. Si doping is also tested because it is commonly used to increase electron conductivity for n-doped hematite.[11,13] For anion substitutions, F doping is tested by substituting it in for a terminating O. Unlike the terminating O in the hydroxylated surfaces, the terminating F anions do not bond to any H atoms since they are monovalent and only interact with a surface Fe atom. The rest of the paper is organized as follows: section 2 describes the models used for simulating water oxidation on oxide surfaces, section 3 provides computational details, section 4 presents results and discussion, and section 5 concludes.

2. WATER OXIDATION REACTION

We adopt the following reaction mechanism scheme[53−55] to identify fundamental aspects of water splitting reactions, in particular water oxidation:

$$H_2O + * \rightarrow *OH_2 \tag{A}$$

$$*OH_2 \rightarrow *OH + H^+ + e^- \tag{B}$$

$$*OH \rightarrow *O + H^+ + e^- \tag{C}$$

$$H_2O + *O \rightarrow *OOH + H^+ + e^- \tag{D}$$

$$*OOH \rightarrow O_2 + * + H^+ + e^- \tag{E}$$

The lone "*" represents a surface with one O vacancy site in the topmost layer. The symbols "*OH$_2$", "*OH", "*O", and "*OOH" represent the surface with the corresponding chemisorbed species residing in the O vacancy site. The mechanism involves four oxidation steps (steps B−E), each of which results in a proton ejected into the electrolyte that will eventually meet a transferring electron at the cathode. H$_2$O first adsorbs onto the surface O vacancy site. The *OH$_2$ species

then undergoes two subsequent oxidation reactions to form *O. Another oxidation step allows *O to react with another water molecule to form the *OOH intermediate. In the last oxidation, O_2 is released from the *OOH. We obtain the energy of $H^+ + e^-$ implicitly by referencing it to the energy of H_2 using the standard hydrogen electrode (SHE, $^1/_2 H_2 \rightarrow H^+ + e^-$, at pH = 0, p = 1 atm, T = 298 K). Applying an external bias ϕ on the proton-coupled electron transfer processes in reactions B−E is accounted for by including a $-e\cdot\phi$ term in their reaction free energies. For example, when ϕ = 0 at standard conditions, the free energy of reaction C is the same as the free energy of the reaction *OH $\rightarrow$ *O + $^1/_2 H_2$. Other electrochemical models explicitly simulate electrostatic responses to a constant field, or they generate an electric field via charged slabs and then compensate the extra charges with a uniform charge compensating background.[56−60] In theoretical studies on water oxidation and oxygen reduction on Pt (111), these three models gave similar results.[57] Here, we adopt the first and simplest model, which has also been applied to examine water oxidation on other metal oxide surfaces.[55] Deviations from the standard pH = 0 condition can be treated by adding a $-kT \ln 10 \cdot pH$ correction, where k is the Boltzmann constant. Zero point energy (ZPE) and entropic contributions are also calculated or taken from standard tables (see Computational Details section). Enthalpy changes due to temperature increasing from 0 to 298 K are expected to be small and are normally neglected.[53−55] Therefore, the reaction free energies are calculated as follows:

$$\Delta G_A = E(*OH_2) - E(*) - E_{H_2O} + (\Delta ZPE - T\Delta S)_A \tag{1}$$

$$\Delta G_B = E(*OH) - E(*OH_2) + {}^1/_2 E_{H_2} \\ + (\Delta ZPE - T\Delta S)_B - e\cdot\phi \tag{2}$$

$$\Delta G_C = E(*O) - E(*OH) + {}^1/_2 E_{H_2} \\ + (\Delta ZPE - T\Delta S)_C - e\cdot\phi \tag{3}$$

$$\Delta G_D = E(*OOH) - E(*O) - E_{H_2O} + {}^1/_2 E_{H_2} \\ + (\Delta ZPE - T\Delta S)_D - e\cdot\phi \tag{4}$$

$$\Delta G_E = E(*) - E(*OOH) + E_{O_2} + {}^1/_2 E_{H_2} \\ + (\Delta ZPE - T\Delta S)_E - e\cdot\phi \tag{5}$$

E_{H_2O}, E_{H_2}, and E_{O_2} are the calculated energies for the isolated gaseous molecules H_2O, H_2, and O_2, respectively. Because ΔG_A is not an oxidative process, it does not depend on ϕ. Following Nørskov et al.,[53,61] we define the reaction potential, ϕ_{rx}, as the potential that makes all individual voltage-dependent steps (reactions B−E) have ΔG values ≤ 0. Therefore, ϕ_{rx} is equal to the most positive value among ΔG_B, ΔG_C, ΔG_D, and ΔG_E. The effective binding energies of O, OH, and OOH species at the surface O vacancy site, are calculated as[55]

$$\Delta G_{*O} = E(*O) - E(*) - E_{H_2O} + E_{H_2} + \Delta ZPE - T\Delta S \tag{6}$$

$$\Delta G_{*OH} = E(*OH) - E(*) - E_{H_2O} + {}^1/_2 E_{H_2} \\ + \Delta ZPE - T\Delta S \tag{7}$$

$$\Delta G_{*OOH} = E(*OOH) - E(*) - 2E_{H_2O} + {}^3/_2 E_{H_2} \\ + \Delta ZPE - T\Delta S \tag{8}$$

Lastly, the (average) H adsorption energy on the O-terminated surface is evaluated as

$$G_{ad} = [E(\text{O-terminated slab} + n\text{H}) \\ - E(\text{O-terminated slab}) - (n/2)E_{H_2}]/n \\ + \Delta ZPE - T\Delta S \tag{9}$$

where n is the number of H atoms adsorbed onto the O-terminated surface.

3. COMPUTATIONAL DETAILS

In this section, we provide a brief description of the computational models used. More technical details can be found in Supporting Information, along with total energies and coordinates of all molecules in their equilibrium geometries. We used the VASP program (version 5.2)[62,63] for all calculations. The Perdew, Burke, and Ernzerhof (PBE)[64] GGA XC functional was employed. All-electron frozen core PAW potentials[65,66] were used for the ion-electron terms ("ion" refers to a nucleus screened by its core electrons). Spin-polarized DFT+U theory was used to properly describe the antiferromagnetism of hematite and to correct the DFT SIEs for strongly correlated electrons in the first-row transition metal ions. The efficacy of this theory is evident for our purposes, as it has been shown to predict, for example, more accurate redox potentials and oxidation energies of transition metal oxides than standard DFT.[67,68] We utilized the rotationally-invariant DFT+U formalism proposed by Dudarev et al.[69] and implemented by Bengone et al.[70] DFT+U predictions can depend on the value used for $U - J$, the one parameter in the theory, which represents the spherically averaged intra-atomic Coulomb minus exchange energy of the localized (here d) electrons that suffer the most from SIE. Rather than fit this parameter to match experiment as is frequently done, we use a fully *ab initio* value of $U - J$ = 4.3 eV for Fe that was derived for Fe^{3+} in Fe_2O_3 using a size-converged electrostatically-embedded cluster model within unrestricted Hartree−Fock theory.[71] Our previous work using the *ab initio* derived $U - J$ value (4.3 eV) for hematite showed that DFT+U predicts ground state structures and ground and excited state electronic properties of bulk hematite in very good agreement with experiments, in contrast to DFT alone.[71,72] We also validated the DFT+U method using $U - J$ = 4.3 eV in studies of the two lowest-energy surfaces of hematite.[35] In the present work, two scenarios of $U - J$ values were tested for the other first-row transition metals as dopants. In one case, we used the same $U - J$ = 4.3 eV for all the transition metals, so as to not artificially bias the 3d electron occupations among different transition metal cations. In the other case, we used the $U - J$ derived from experiments or from *ab initio* calculations (5.0 eV for Ti^{4+},[73,74] 3.5 eV for Mn^{2+},[75] 4.0 eV for Co^{3+},[76] and 3.8 eV for Ni^{2+}).[77] Oxygen- and hydrogen-containing species were treated with standard DFT-PBE, since they do not exhibit much SIE; DFT-PBE describes molecular thermochemistry moderately accurately, with a mean unsigned error of 0.17 eV for alkyl bond dissociation energies (ABDE4 database).[78]

The hexagonal unit cell of pure hematite was fully optimized at the PBE+4.3 (shorthand notation for using the PBE XC functional and $U - J$ = 4.3 eV) level, leading to predicted lattice vectors a = 5.10 Å and c = 13.92 Å, both of which are within 1% of the experimental values of a = 5.04 Å and c = 13.75 Å.[22] (1×1) and (2×2) slab models of four stoichiometric units (~9.3 Å thick, see Figure 1) were built from the optimized bulk crystal structure. These two slabs of different lateral sizes are used to evaluate the dependence of reaction energetics on different concentrations of surface reaction sites (1/3 ML in the (1×1) slab compared to 1/12 ML in the (2×2) slab). Given the complex nature of a hematite electrode surface under hydrating conditions (due to polycrystalline facets, vacancies, and hydroxylation), we expect the actual surface to have more rather than less reactive sites. Thus, we

believe that the (1×1) slab that represents a higher concentration of reactive sites is more likely to be representative of the actual reaction conditions. Reactive species were introduced on both sides of the slab so the slab had no net dipole moment. In subsequent structural optimizations of the periodic slabs, the lateral lattice vectors were held fixed, while the ion positions were allowed to relax. A vacuum layer at least 10 Å thick (measured from wherever the slab or the water molecules end) was used to isolate slabs from their periodic images. Bader charges were calculated by integrating electron densities within zero flux surfaces around nuclei and are converged to within 0.1 e compared to a grid 1.5 times denser along each lattice vector.[79] The valence band maximum (VBM) was evaluated by referencing the energies of the highest occupied bands in the optimized slabs to the electrostatic potential energy in the vacuum region.

Doping effects on surface chemistry were tested by direct cation or anion substitutions (Figure 1). Substitutions were made at the layers
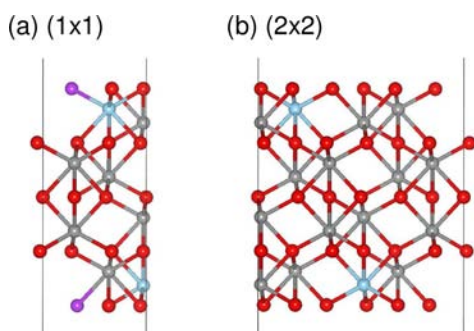
Figure 1. O-terminated Fe_2O_3 (0001) slab models: (a) (1×1) slab with 23 atoms per unit cell and (b) (2×2) slab with 92 atoms per unit cell. O is depicted in red and Fe in gray. The ions for cation and anion substitutions are colored blue and purple, respectively. Only cation substitution was tested for the (2×2) slab.

nearest to the surface, directly bonding to the reactive site, to simulate the maximum effect of doping on surface reactions. We expect the influence of the dopant will diminish when the dopant atom is located farther from the reaction site. Thus, predictions for a distribution of dopant locations should fall between the limits studied here of pure hematite and having a dopant adjacent to the reaction site. Two different dopant concentrations were tested in which the cation dopant substitutes either one out of two (or one out of eight) Fe cations within the Fe bilayer in the (1×1) (or (2×2)) slab. The anion dopant replaces one out of three O anions in the terminating O layer in the (1×1) slab (anion substitution in the (2×2) case encountered convergence difficulties and is not reported). The magnetic moments of the substituting cations were set to follow the same sign as those of the Fe cations being substituted. We also tested another scenario with the dopants having magnetic moments opposite to the Fe cations being substituted. The energy differences between these two scenarios are small (<0.01 eV/atom), and the first scenario is lower in energy for most species.

ZPE and entropic contributions are presented for individual species in Table 1 and for individual reactions or binding energies in Table 2. The ZPE corrections were obtained from vibrational frequencies derived from Hessians calculated from finite differences of analytic gradients on single molecules in vacuum or adsorbates on (1×1) pure hematite slab models. The ZPE corrections calculated by Valdés et al.[54] using DFT-GGA for related reactive species on the rutile TiO_2 (110) surface are included in Table 1 for comparison. The ZPE corrections calculated for reactive species on the Fe_2O_3 (0001) surface are very close to those for the TiO_2 (110) surface, with differences ≤0.07 eV. This similarity suggests that the vibrational frequencies of O–O and O–H bonds do not change significantly for different metal oxide substrates.

The entropic contributions for gaseous molecules are taken from standard thermodynamics tables.[80] The entropic contributions to the

Table 1. Entropic Energy Contributions (T = 298.15 K) and ZPE Corrections for Gaseous and Adsorbed Molecules and Reactive Species on Hematite (0001)^a

	TS [eV]	ZPE [eV]	ZPE for TiO_2 [eV][54]
$H_{2(g)}$	0.40	0.27	0.27
$O_{2(g)}$	0.63	0.10	0.10
$H_2O_{(l)}$	0.67	0.57	0.56
*O	0	0.04	0.05
*OH	0	0.37	0.35
*OOH	0	0.48	0.41
$*OH_2$	0	0.67	0.70

^{a}See text for details about how the TS term for H_2O is calculated.

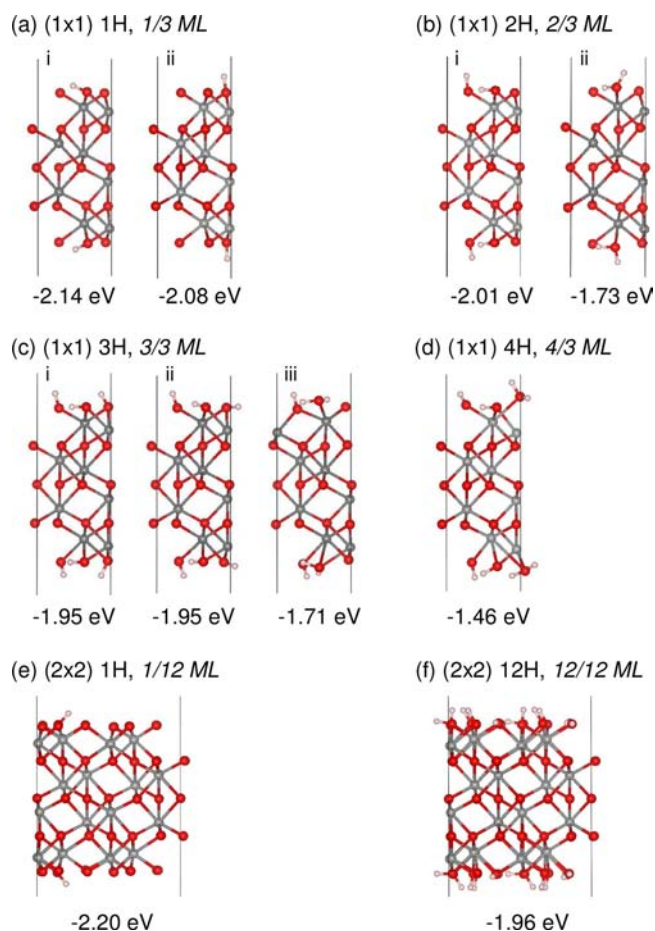**Table 2. Entropic Energy Contributions (T = 298.15 K) and ZPE Corrections for Reaction Steps A–E and Adsorbate Binding Energies, $\Delta G_{adsorbate}$^{a}**

	ΔZPE $- T\Delta S$ [eV]
reaction A	0.77 (0.10)
reaction B	−0.37
reaction C	−0.39
reaction D	0.47
reaction E	−1.08 (−0.41)
ΔG_{*O}	0.01
ΔG_{*OH}	0.40
ΔG_{*OOH}	0.48

^{a}Values in parentheses for reactions A and E have a water molecule from the water layer bound to the O vacancy site in the otherwise clean "*" species, effectively making this intermediate an $*OH_2$ species (see bottom of Figure 3).

total energy of a water molecule in solution is evaluated as the entropic contribution to the energy of a gas-phase water molecule minus the condensation energy from gas to liquid for water at 298.15 K. This scheme enables us to physically model the absolute energy of a water molecule in the liquid phase including solvation and standard state corrections. Entropic contributions from absorbed species on the surfaces are small, so they are usually omitted,[53,61] as we do here. For H adsorption, ΔZPE values in eq 9 for different coverages of H are calculated to be close to 0.18 eV with deviations <0.01 eV. Since the entropic contributions from slabs with H adsorption are omitted, the $-T\Delta S$ term in eq 9 is 0.20 eV (one-half of that for the H_2 molecule, see Table 1). Therefore, the ΔZPE $- T\Delta S$ term in eq 9 is set to 0.38 eV.

4. RESULTS AND DISCUSSION

4.1. H Adsorption on the O-Terminated Fe_2O_3 (0001) Surface. We began our investigation by obtaining equilibrium structures for the fully hydroxylated Fe_2O_3 (0001) surface via H adsorption on the O-terminated Fe_2O_3 (0001) surface. The H atoms adsorbed onto this surface form terminating OH groups that can adopt different orientations in which the H lies nearly within the O planes (e.g., Figure 2a-i) or on top of the O anions (Figure 2a-ii). Initially, the slabs with adsorbed H were built by adding H atoms manually to the slab. Depending on the starting geometry, the optimized structures varied in total energies, and the H atoms relaxed into different and seemingly arbitrary positions on the two sides of the slab. To systematically investigate the energetics of H adsorption and obtain minimum energy structures, a two-dimensional 7×7 grid of points on the (1×1) slab was used as initial positions for the adsorbed H atoms. The grid spacing is sufficiently dense (a

(a) (1×1) 1H, *1/3 ML*

-2.14 eV   -2.08 eV

(b) (1×1) 2H, *2/3 ML*

-2.01 eV   -1.73 eV

(c) (1×1) 3H, *3/3 ML*

-1.95 eV   -1.95 eV   -1.71 eV

(d) (1×1) 4H, *4/3 ML*

-1.46 eV

(e) (2×2) 1H, *1/12 ML*

-2.20 eV

(f) (2×2) 12H, *12/12 ML*

-1.96 eV

Figure 2. Optimized geometries of the O-terminated Fe_2O_3 (0001) surfaces with different coverages of H atoms. For each coverage, the lowest-energy structure is shown on the left. The unit cell size, number of H atoms, and coverage of H atoms is listed above each figure. "ML" means monolayer. The average H adsorption energy is given below each figure. Figures depict O in red, Fe in gray, and H in pink. This color scheme is used throughout.

distance of ∼0.73 Å between nearby points) to sample important positions on the surface, such as those on top of O anions and those at equal distances to adjacent O anions. The (1×1) slab (four stoichiometric units thick) is thick enough so that scanning along different H positions on one side of the slab does not influence the bonding of the H on the other side of the slab. Furthermore, although the entire slab itself does not have internal mirror symmetry, the atoms comprising the terminating O layers and their nearest Fe bilayers at each slab surface are nearly symmetric to each other (Figure 1a). This means that H atoms aligned on opposite sides of the slab encounter almost the same bonding potential, meaning scans for both sides of the slab can proceed simultaneously. For the first scan, H atoms were added to opposite sides of the slab at one of the 7×7 grid points (at starting positions 0.8 Å away from the terminating O layers). The structures were then fully optimized for all 49 points. The lowest-energy structure was then used in subsequent scans at higher coverage adding H atoms to each side of the new slabs in the same manner as before. Since the outermost atoms terminating the slabs are now H atoms, the starting positions for the subsequent, higher coverage PES scans are closer (0.5 Å away from the terminating atoms) to prevent the newly added

H from being too far away from the outermost O layers. Following this procedure, we obtained the lowest-energy structures with up to four H atoms on each side of the slab (4/3 ML, corresponding to four H atoms over three O anions in each terminating layer). Due to steric repulsion, ion relaxations from a (1×1) slab with five H atoms on each side resulted in water desorption, so H coverages >4/3 ML were not considered further.

The optimized geometries with different H coverages and the corresponding average H adsorption energies (see eq 9) are displayed in Figure 2. The minimum energy geometry with one H adsorbed on each side of the (1×1) O-terminated surface (1/3 ML) has O−H bonds lying nearly flat toward the terminating O layers (Figure 2a-i). This is the preferred orientation due to maximal hydrogen bonding between −OH to nearby terminating O anions. Having the O−H bond pointing away from the surface (see Figure 2a-ii) produces a structure higher in energy by 0.06 eV. When two H atoms are adsorbed on each side of the (1×1) slab (2/3 ML, Figure 2b-i), the lowest-energy structure has two H atoms bonding to two different O anions. The slab with a bound −OH_2 molecule (Figure 2b-ii) is 0.28 eV higher in energy. When three H atoms are bound on each side of the slab (1 ML), we find two structures consisting of three −OH groups on each side, each with different numbers of O−H bonds pointing toward vacuum (Figure 2c-i and -ii). Close competition between hydrogen bonding attractions and steric repulsions makes these two geometries essentially degenerate in energy. A third possible geometry with 1 ML coverage has 2 H atoms bonded to the same O (Figure 2c-iii), but this is 0.24 eV higher in energy, as was found with the 2/3 ML case. Interestingly, deviations between the geometric positions of Fe and O ions in the slab with those in the bulk structure *decrease* as the number of H *increases* from one to three. Dangling bonds from the terminating O anions become passivated once O−H bonds are formed, such that the fully hydroxylated slab becomes bulk-like in terms of both geometry and electronic structure. As expected, O−H bond lengths are predicted to be ∼1.0 Å in all cases. On the basis of our results from the (1×1) slab which showed the formation of −OH groups is preferred to −OH_2 groups, we optimized the geometry for the (2×2) slab using 1 H atom (1/12 ML) and 12 H atoms (1 ML) on each side of the slab. The lowest-energy structure of the (2×2) slab with 1 ML of H has half of the O−H bonds lying nearly flat with respect to the terminating O plane while the other half are pointing away toward the vacuum region away from the slab.

Regardless of H coverage, all H adsorption energies are negative, suggesting that the hydroxylated Fe_2O_3 (0001) slab is energetically more favorable than the O-terminated Fe_2O_3 (0001) slab. Due to increased steric repulsion, H adsorption energies slightly decrease as the number of H atoms increases. Increasing the slab dimension from (1×1) to (2×2) decreases the isolated H adsorption energy by only 0.06 eV (going from 1/3 to 1/12 ML), suggesting that the structure with one H adsorbed on the (1×1) slab model (1/3 ML) is already sufficiently modeling the low coverage limit. As expected, at 1 ML coverage both the (1×1) and (2×2) slabs give similar H adsorption energies of ∼ −2.0 eV, differing by only 0.01 eV. This implies the (2×2) slab with 1 ML coverage is like a supercell of the (1×1) slab with 1 ML coverage, as expected, with the two orientations of the OH groups (lying nearly flat or pointing away from the slab) being so close in energy that they both are likely to be present on the surface.
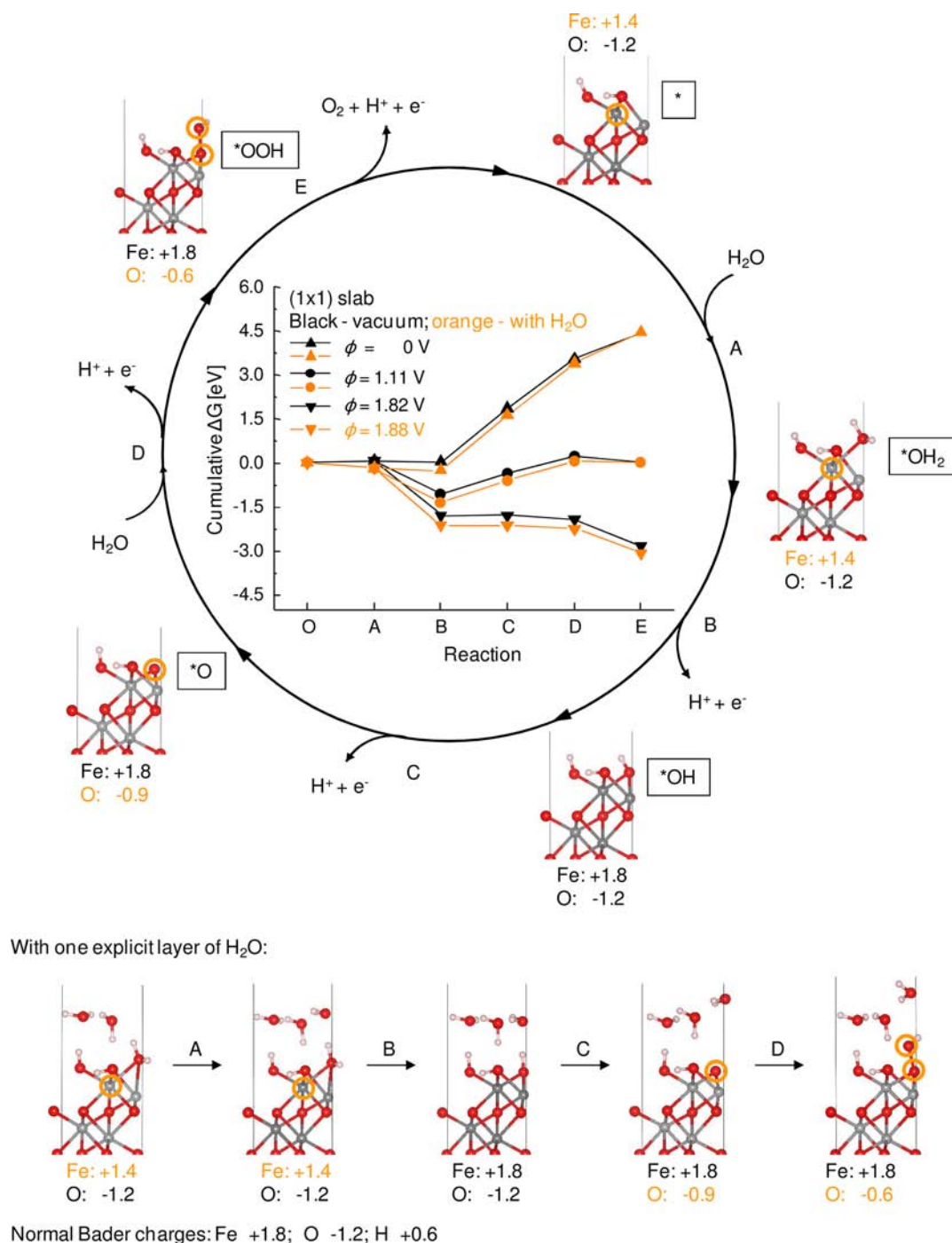
Figure 3. Schematic illustrations of the water oxidation reaction pathway on hematite showing optimized structures for all intermediates under vacuum. The terminating ions with unusual Bader charges are highlighted with orange circles, and their values are reported below each figure in orange. Cumulative free energies of reactions (ΔG_{298}, normalized to the formation of one oxygen molecule) are plotted in the center of the reaction cycle. "O" under the x-axis represents the state consisting of the hematite surface containing one oxygen vacancy plus two water molecules in the liquid state. Line segments connect the adjacent reactions. For example, the line segment A–B illustrates the free energy for reaction B. The optimized geometries of reactive intermediates with a water overlayer are shown at the bottom. For clarity, we illustrate the reaction intermediates on one side of the slab even though our models consider reactions on both sides of the slab. Normal Bader charges for Fe and O are derived from hematite bulk calculations. Normal Bader charges for H are derived from the *OH species, which exhibits hematite bulk-like geometry and electronic structure.

4.2. Water Oxidation Reactions on the Fully Hydroxylated Fe$_2$O$_3$ (0001) Surface.

The minimum energy structures obtained by optimizing O-terminated slabs with different H coverages (as described above) are used as *O, *OH, and *OH$_2$ intermediates. Initial structures for *OOH and "*" were built manually starting from the optimized slabs at 2/3 ML H-coverage and then they were fully relaxed to energy minima. The reaction pathway intermediates and the Bader charges for their surface ions are displayed in Figure 3. Here, water oxidation is illustrated as a continuous catalytic cycle. Starting at

the top right, the reactant of reaction A, "*", has one O vacancy in the terminating O layer. As a result, the Fe cation in the orange circle closest to the O vacancy is less ionic with less positive charge than normal (charges deviating from bulk values are shown in orange). In reaction A, one water molecule is adsorbed onto the surface at the O vacancy site, forming *OH_2. Since the water molecule is charge-neutral, the Fe cation remains in its lower oxidation state. In reaction B, one proton and one electron leave the surface (in a real system, the proton to the electrolyte and the electron into the hematite bulk crystal and out to an external circuit), producing the bulk-like fully hydroxylated Fe_2O_3 (0001) surface without any unusual Bader charges. In reaction C, the surface undergoes another oxidative process with another proton and electron removed. According to Bader analysis, the resulting hole resides on the deprotonated O anion. In reaction D, the *OOH product is formed by addition of water and loss of a proton and an electron, with both O anions in the −OOH group having less negative charge than the other O anions. In reaction E, one O_2 molecule is released along with one proton and one electron.

The cumulative reaction free energies (ΔG_{298}) for the proposed reactions steps are plotted in the center of Figure 3 and given in Table 3. We first analyze the gas-phase energetics.

Table 3. Free Energies of Reactions (ΔG_{298}, in eV) without External Bias ($\phi = 0$) and Reaction Potentials (ϕ_{rx}, in V) for Water Oxidation on the Fully Hydroxylated, Pure Fe_2O_3 (0001) Surface[a]

	(1×1) 1/3 ML reactive sites		(2×2) 1/12 ML reactive sites
	vacuum	with H_2O	vacuum
ΔG_{298}(A)	0.05 (−0.72)	−0.20 (−0.30)	0.19 (−0.58)
ΔG_{298}(B)	−0.03 (0.34)	−0.07 (0.30)	−0.16 (0.22)
ΔG_{298}(C)	*1.82 (2.21)*	*1.88 (2.27)*	*2.02 (2.41)*
ΔG_{298}(D)	1.69 (1.22)	1.77 (1.30)	1.43 (0.96)
ΔG_{298}(E)	0.90 (1.98)	1.05 (1.46)	0.95 (2.03)
ϕ_{rx}	1.82 (2.21)	1.88 (2.27)	2.02 (2.41)

[a]Numbers in parentheses are reaction energies omitting ZPE and entropic corrections. The most positive reaction energies within each column (equal to ϕ_{rx}) are in bold italic. The coverages refer to the concentration of oxygen vacancies at each surface.

With no applied external potential ($\phi = 0$ V), the cumulative ΔG_{298} for all reactions is 4.43 eV, the DFT-GGA-PBE calculated water splitting reaction energy ($2H_2O_{(l)} \rightarrow O_{2(g)} + 2H_{2(g)}$). The predicted electrochemical reaction potential is then 1.11 V (4.43 eV/4e = 1.11 V), a value in reasonable agreement with measured water splitting reaction potential of 1.23 V. The most endoergic step is reaction C. At an external potential ϕ of 1.11 V, the overall ΔG_{298} for the reaction is zero. At this applied potential, the only endoergic steps are C and D. Recall that since reaction A does not involve an oxidation step, it is independent of ϕ. Increasing the applied potential further to $\phi_{rx} = 1.82$ V causes the ΔG_{298} values of all electrochemical reactions B−E to be ≤0. The lower limit of the overpotential is then approximated as the difference between this 1.82 V value and the calculated water reaction potential of 1.11 V, which is equal to 0.71 V. Since the overpotential is a consequence of electrochemical kinetic barriers, it is appropriate to use kinetic schemes incorporating potential-dependent reaction barriers to obtain overpotentials.[81,85] However, such barriers are challenging to calculate from first principles, and lower bounds to the

overpotential provided by this simpler thermodynamic analysis has been demonstrated to satisfactorily predict experimental overpotentials for other electrocatalytic reactions.[53,61]

Solvent effects are considered by adding a water overlayer (consisting of three water molecules for the (1×1) slab) on both sides of the slab. Earlier studies by Rossmeisl et al. considered multiple layers of water to simulate the interface between an electrolyte and an electrified Pt (111) surface.[59] They found a single water layer capably described the variation of potential through the interface, suggesting that for flat surfaces such as the basal plane of hematite, a monolayer of water may be sufficient to capture both electrostatics and H bonding interactions. The initial geometries of the water layer were chosen manually, and they were built to maximize hydrogen bonding between the water layer and the surface O(H) species to assess the maximum perturbation caused by the water layer. The final optimized geometries are shown at the bottom of Figure 3. The cumulative ΔG_{298} for reactions with a monolayer of water on top is also plotted in Figure 3 in orange. The lines connecting reactions A−D under vacuum conditions and with the H_2O monolayer are nearly parallel, implying nearly the same ΔG_{298} for the individual reaction steps B, C, and D. Indeed, this solvation model mainly affects reactions A and E. As previously stated, when the surface with the O vacancy (*) is in contact with the water layer, a water molecule chemisorbs into the oxygen vacancy. This reduces the ΔG_{298} for reaction A by 0.35 eV and increases the ΔG_{298} for reaction E by 0.25 eV. The reaction potential ϕ_{rx} with the water layer is 1.88 V, only 0.06 V higher than the case under vacuum. As discussed in the Computational Details section, we believe that this model for water oxidation (using the (1×1) hydroxylated hematite slab with 1/3 ML reactive sites with an additional overlayer of water molecules) is most representative of experimental conditions. The overpotential of 0.77 V predicted is in reasonable agreement with the 0.5−0.6 V range measured for hematite photoanodes.[5]

ΔG_{298} values for the individual water oxidation reaction steps on the (1×1) and (2×2) slabs are provided in Table 3. The (1×1) slab (with 1/3 ML reactive sites) and the (2×2) slab (with 1/12 ML reactive sites) provide a measure of the reaction energy dependence on surface reactive site concentrations. The ΔG_{298}s for the (2×2) slab under vacuum are comparable to those for the (1×1) slab under vacuum, with differences ≤0.26 eV. The overall reaction potential for the (2×2) slab under vacuum is 0.2 V higher than the one for the (1×1) slab under vacuum. This similarity suggests that the reaction on the surface is fairly localized and exhibits only a small coverage dependence.

4.3. Water Oxidation Reactions on the Fully Hydroxylated Fe_2O_3 (0001) Surface with Dopants. Table 4 presents the reaction free energies and reaction potentials for water oxidation on the doped, fully hydroxylated hematite (0001) surfaces under vacuum and explicitly solvated conditions. The cation or anion dopants are bonded directly or positioned adjacent to the reaction site (see Figure 1 and text in the Computational Details section for more details). Unlike Table 3, we only report ΔG_{298} values with ZPE and entropic corrections. The reaction energies without ZPE and entropic corrections can be derived using corrections listed in Table 2. We first analyze results from the (1×1) slab models. In vacuum and employing the $U − J$ values appropriate for different dopants discussed earlier, the ϕ_{rx} values for doped surfaces follow the ordering: Ni < Co < F < Mn < Si < Ti. The ϕ_{rx}

Table 4. Free Energies of Reactions (ΔG_{298}, in eV) without External Bias ($\phi = 0$) and Reaction Potentials (ϕ_{rx}, in V) for the Water Oxidation Reaction on the Doped Fully Hydroxylated (1×1) and (2×2) Fe$_2$O$_3$ (0001) Surfaces[a]

	dopant					
	Ti	Mn	Co	Ni	Si	F
	(1×1) 1/3 ML Reactive Sites—Vacuum					
$U - J$ [eV]	5.0	3.5	4.0	3.8	–	–
ΔG_{298}(A)	−0.08	0.04	0.07	0.00	0.44	−0.10
ΔG_{298}(B)	−0.38	0.37	0.75	0.99	−0.40	−0.02
ΔG_{298}(C)	0.23	1.00	*1.74*	1.66	0.51	*2.08*
ΔG_{298}(D)	*3.27*	*2.49*	1.61	*1.67*	*2.92*	1.56
ΔG_{298}(E)	1.39	0.54	0.26	0.11	0.97	0.92
ϕ_{rx}	3.27	2.49	1.74	1.67	2.92	2.08
$U - J$ [eV]	4.3	4.3	4.3	4.3		
ΔG_{298}(A)	−0.05	0.02	0.06	−0.01		
ΔG_{298}(B)	−0.53	0.54	0.85	1.08		
ΔG_{298}(C)	0.20	1.18	*1.77*	*1.73*		
ΔG_{298}(D)	*3.29*	*2.31*	1.59	1.61		
ΔG_{298}(E)	1.53	0.38	0.16	0.03		
ϕ_{rx}	3.29	2.31	1.77	1.73		
	(1×1) 1/3 ML Reactive Sites—with H$_2$O					
$U - J$ [eV]	5.0	3.5	4.0	3.8	–	–
ΔG_{298}(A)	−0.16	−0.16	−0.23	−0.27	−0.20	−0.21
ΔG_{298}(B)	−0.44	0.23	0.82	1.11	−0.65	−0.04
ΔG_{298}(C)	0.35	1.08	*1.80*	1.75	0.58	*2.36*
ΔG_{298}(D)	*3.32*	*2.57*	1.71	1.73	*3.07*	1.28
ΔG_{298}(E)	1.36	0.72	0.33	0.11	1.63	1.04
ϕ_{rx}	3.32	2.57	1.80	1.75	3.07	2.36
	(2×2) 1/12 ML Reactive Sites—Vacuum					
$U - J$ [eV]	5.0	3.5	4.0	3.8	–	
ΔG_{298}(A)	−0.13 (−0.13)	0.15	0.17	0.11	0.32	
ΔG_{298}(B)	−0.44 (−0.24)	0.19	0.67	0.92	−0.66	
ΔG_{298}(C)	0.25 (0.04)	1.06	*1.70*	*1.67*	0.61	
ΔG_{298}(D)	*3.30 (3.38)*	*2.37*	1.63	1.64	*2.94*	
ΔG_{298}(E)	1.45 (1.37)	0.67	0.26	0.09	1.22	
ϕ_{rx}	3.30 (3.38)	2.37	1.70	1.67	2.94	

[a]The most positive reaction energies within each column (equal to ϕ_{rx}) are in bold italic. Ti doping can occur in two different ways with the lower coverage (2×2) slab: values not in parentheses are for the Ti^{4+}/Fe^{2+} scenario that exists also for the higher coverage (1×1) slab, and values within parentheses are for the Ti^{3+}/Fe^{3+} scenario that only occurs at the lower coverage. See text for details.

values for Ni- and Co-doped surfaces are smaller than for a pure hematite surface. The Ti-doped surface has the largest ϕ_{rx}, which is 1.45 V higher than for the pure hematite surface. When all dopants have the same $U - J = 4.3$ eV as Fe, the above trend still holds. The ΔG_{298} and ϕ_{rx} are similar in the two cases (using $U - J$ values appropriate for individual dopants or same $U - J = 4.3$ eV for all) and have a largest difference of 0.18 eV for ΔG_{298} and 0.18 V for ϕ_{rx}. Table 4 also shows results from the (2×2) slab model under vacuum, employing different $U - J$ values appropriate for different dopants. These data correspond to lowering the dopant concentration from 1/2 in the Fe bilayer of the (1×1) slab to 1/8 in the Fe bilayer of the (2×2) slab, as well as lowering the concentration of reactive sites from 1/3 to 1/12 ML. The predictions exhibit only a small dependence on the concentrations of dopants or reactive sites, with a largest difference of 0.26 eV for ΔG_{298} and 0.12 V for ϕ_{rx}. Therefore, similar to what is found for pure hematite in the previous section, the reaction is quite spatially localized and most sensitive to changes at adjacent sites.

We now focus on further analyzing dopant effects resulting from the model employing appropriately different $U - J$ values. Including one layer of water has a similar effect on doped

surfaces as with pure hematite (Table 4). The ϕ_{rx} changes less than 0.1 V in all cases except for Si and F, which increase by 0.15 and 0.28 V, respectively. To test the dependence of ϕ_{rx} on dopant concentrations, results for Ti, Mn, Co, Ni, and Si doping in the (2×2) slab models are also presented in Table 4. Calculations on F doping did not consistently converge properly for the larger (2×2) supercell, and therefore they are not reported.

Dopants retain similar charges in the (1×1) and (2×2) slabs in all cases except Ti. The latter can have either a +4 or a +3 charge when near the *OH and *OOH species at the lower coverage afforded by the (2×2) slab. When Ti has a +4 charge, a nearby Fe^{3+} cation is reduced to Fe^{2+} (just as for Ti doping in the (1×1) slab, *vide infra*). When Ti has a +3 charge, all the Fe cations have +3 charges. The *OH (or *OOH) with a nearby Ti^{3+} is higher in energy by 0.21 (or 0.08) eV than that with a nearby Ti^{4+}, resulting in a 0.08 V difference in ϕ_{rx} between the Ti^{4+}/Fe^{2+} and Ti^{3+}/Fe^{3+} scenarios. Since the energy difference between these two cases depends on the $U - J$ values used for Fe and Ti, we report results for both (2×2) slab scenarios in Table 4. Overall, predictions from (2×2) slabs are very similar to those of the (1×1) slabs, with largest differences being 0.26

13303

dx.doi.org/10.1021/ja301567f | *J. Am. Chem. Soc.* 2012, 134, 13296−13309

Table 5. Bader Charges (q) and Magnetic Moments (μ, in Absolute Values) of the Dopants in the Fully Hydroxylated (1×1) Fe$_2$O$_3$ (0001) Surfaces under Vacuum

reaction intermediate	dopant, $U - J$ [eV]											
	Ti, 5.0		Mn, 3.5		Co, 4.0		Ni, 3.8		Si, −		F, −[a]	
	q_{Ti}	μ_{Ti} [μ_B]	q_{Mn}	μ_{Mn} [μ_B]	q_{Co}	μ_{Co} [μ_B]	q_{Ni}	μ_{Ni} [μ_B]	q_{Si}	μ_{Si} [μ_B]	q_{Fe}/q_F	μ_{Fe} [μ_B]
*	2.0	0.9	1.5	4.5	1.2	2.7	1.2	1.6			1.4/−0.8	3.7
*OH$_2$	2.1	0.9	1.5	4.6	1.3	2.7	1.2	1.7			1.4/−0.8	3.7
*OH	2.3	0.1	1.8	3.8	1.3	0.1	1.3	0.8	3.1	0.0	1.9/−0.7	4.3
*O	2.3	0.0	1.9	3.0	1.4	0.8	1.4	0.0			1.8/−0.7	3.6
*OOH	2.3	0.1	1.7	3.8	1.3	0.0	1.3	0.9			1.8/−0.7	4.2

[a] For F doping, the charges and magnetic moments of the Fe in the cation substitution sites are given.

eV for individual ΔG_{298} values and only 0.12 V for ϕ_{rx}. These small differences suggest that the water oxidation reaction on hematite surface depends primarily on the local chemical environment and does not drastically change with the dopant concentration. This conclusion should also apply to F doping.

Table 5 reports the Bader charges and magnetic moments of dopants placed as nearest neighbors to the reactive O vacancy sites in the (1×1) slabs to discern their maximum effect. The charges and magnetic moments of Fe in the pure hematite surface are nearly identical to those of F doping and have a maximum difference of 0.1 in charge or 0.1 μ_B in magnetic moment. The changes in charges of cation dopants for different surface reaction intermediates follow similar trends to what was found above for the pure hematite surface, but they are smaller in magnitude for Ti, Co, and Ni. The charges on the dopants in the * and *OH$_2$ species are smaller than the charges on the dopants with the other three reactive species present. Si dopants are an exception to this, however. Here, the charge on Si remains +3.1 throughout the catalytic reaction cycle, while O anions become more negatively charged compared to O anions in pure or other cation-doped hematite surfaces due to Si being electropositive.

We now analyze the oxidation states and electronic configurations of the dopants by combining information extracted from Bader charges, magnetic moments, and projected densities of states (PDOS). Since the fully hydroxylated surface (*OH) is the most bulk-like, we focus on the PDOS of the pure and doped hematite slabs containing the *OH species (Figure 4). In pure hematite, the Fe^{3+} cations are in high-spin d^5 states. (Recall that first-row transition metals first give away their 4s electrons upon ionization, followed by ionization of their 3d electrons.) The occupied states below the Fermi energy are of mixed Fe 3d and O 2p character, while the majority of Fe 3d states have energies below ∼ −6 eV. For both Ti- and Si-doped hematite, one minority Fe 3d peak appears right below the Fermi energy. This peak suggests the existence of Fe^{2+} cations with one minority spin 3d electron, which result from cation substitution by Ti^{4+} or Si^{4+}. The higher oxidation states of Ti and Si compared to other cations are evident from the Bader charges of Ti and Si in Table 5. A Co dopant can adopt oxidation states of either +2 or +3. We tested different initial magnetic moments for Co ions; calculations converged to two possible configurations for the 3d electrons on Co, namely, the high-spin and low-spin cases. We always adopt the spin state species with the lowest energy for reaction energy calculations. In the presence of *OH, the PDOS of Co has nearly symmetric majority and minority occupied 3d states, which, along with its 0.1 μ_B magnetic moment, implies that Co is in the +3 oxidation state of low-spin d^6. Co's magnetic

moment of 2.7 μ_B in the presence of * and *OH$_2$ suggests that for these species Co prefers a high-spin d^7 electronic configuration with a +2 oxidation state. The PDOS of Ni shows more occupied majority states than minority states, and both are partially filled. The PDOS, together with the 0.8 μ_B magnetic moment for Ni, suggests that Ni in the presence of *OH has a low-spin d^7 electronic configuration with a +3 oxidation state. The magnetic moment of ∼1.6 μ_B in * and *OH$_2$ suggests that Ni has a high-spin d^8 electronic configuration with a +2 oxidation state when these species are present. However, the charges of Co and Ni in Table 5 do not vary significantly, and all are smaller than that of Fe. We consider the magnetic moment derived from spin density differences to be a more sensitive measure of electron density around the cation. The Bader charges change little because the electron being added or removed is shared between Co/Ni and O, implying covalent character in Co−O and Ni−O bonds and intermediate charges between +2 and +3 for Co and Ni. For Mn, the similar Bader charges for Mn and Fe suggests that Mn is in the +2 oxidation state in the presence of * and *OH$_2$, and in the +3 oxidation state in the presence of *OH, *O, and *OOH. From the PDOS of Mn in the presence of *OH, the majority Mn 3d states are only partially filled, with unoccupied majority states appearing near the conduction band minimum. Along with a magnetic moment of 3.8 μ_B, this implies that Mn is in +3 oxidation state in the presence of *OH. These charge assignments for Ti, Mn, Co, and Ni agree with previous work by Velev et al.[82] on a transition-metal-doped 30-atom unit cell of hematite using the local density approximation + U method.

Next, we analyze the effects of using different dopants. The cumulative ΔG_{298}s for the case under vacuum with different $U - J$ values for different dopants are plotted in Figure 5 for four different external potentials. From the plots of $\phi = 1.11$ V and $\phi = 2.00$ V, the ΔG_{298} values for reactions C and D show different signs for different dopants. At $\phi = 1.11$ V using pure or Co-, Ni-, or F-doped hematite, reactions C and D are the two most endoergic steps with positive ΔG_C and ΔG_D. At $\phi = 1.11$ V using Ti, Mn, and Si doping, the most endoergic step is reaction D, while all other ΔG_{298} values are slightly positive or are negative. Co or Ni doping each give rise to the lowest ϕ_{rx} and are unique among the other dopants as they exhibit linear energy changes from reactions B−D, such that ΔG_C and ΔG_D are both positive at $\phi = 1.11$ V and both negative at $\phi = 2.00$ V. This means reactions C and D are the key steps for determining ϕ_{rx}. Recall that reaction C corresponds to removing a proton and electron from *OH to form *O, and reaction D corresponds to *O reacting with water to form *OOH. We now focus on characterizing these three different species, *OH, *O, and *OOH.
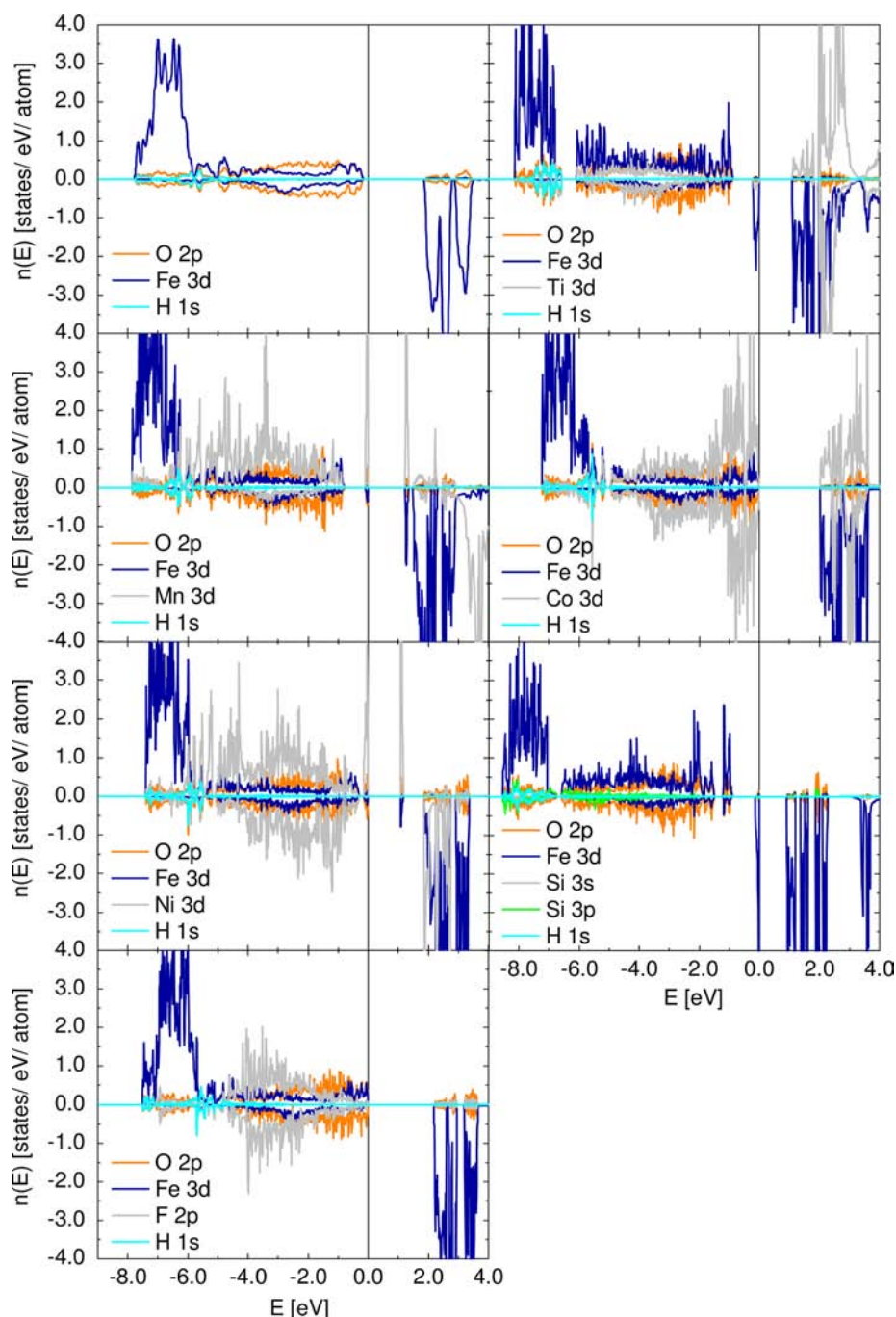
Figure 4. Projected densities of states (PDOS, $n(E)$) for pure and doped fully hydroxylated (1×1) Fe_2O_3 (0001) surfaces under vacuum. Positive values represent majority spin DOS whereas negative values represent minority spin DOS. The DOSs are shifted so that the Fermi level is set to zero, with occupied states at negative energies E (eV).

Scaling relationships among binding energies of *OH, *O, and *OOH have been proposed from studying various transition metal oxide surfaces.[55,83] For example, the differences in binding energies between *OH and *OOH are constant for a series of transition metal oxides.[55] Figure 6a plots the binding energy of *OOH (ΔG_{*OOH} in eq 8) versus that of *OH (ΔG_{*OH} in eq 7) with (in orange) and without (in black) ZPE and entropic corrections. Following Man et al.'s approach,[55] linear fits are obtained by constraining the slope to be 1. The best-fit line with an R^2 value of 0.989 shows the proposed scaling relationship for *OOH and *OH also holds for pure or doped hematite surfaces. Since the key steps determining

reaction potentials are the reactions C and D, the reaction potential with ZPE and entropic corrections follows

$$
\begin{aligned}
\phi_{rx} &= \max(\Delta G_C, \Delta G_D)/e \\
&= \max[(\Delta G_{*O} - \Delta G_{*OH}), (\Delta G_{*OOH} - \Delta G_{*O})]/e \\
&= \max\{(\Delta G_{*O} - \Delta G_{*OH}), [(\Delta G_{*OOH} - \Delta G_{*OH}) \\
&\quad - (\Delta G_{*O} - \Delta G_{*OH})]\}/e \\
&= \max\{(\Delta G_{*O} - \Delta G_{*OH}), [3.464 - (\Delta G_{*O} - \Delta G_{*OH})]\}/e
\end{aligned}
$$

(10)

where 3.464 is the intercept from the linear fitting of the orange curve in Figure 6a. The second line of eq 10 can be derived
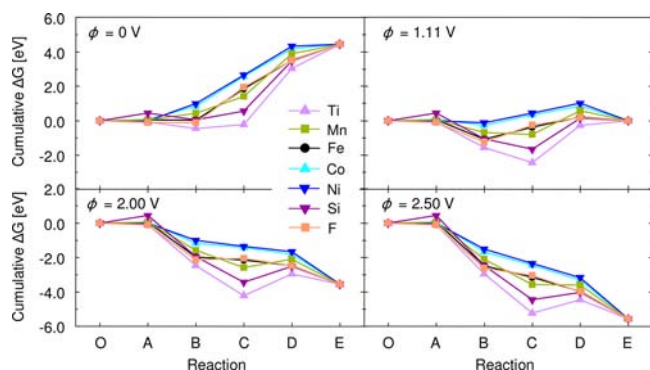
Figure 5. Cumulative free energies of reactions (ΔG) for the pure and doped fully hydroxylated (1×1) Fe_2O_3 (0001) slabs under vacuum at different applied potentials. Different $U - J$ values are used for different first-row transition metal elements. See text for details.
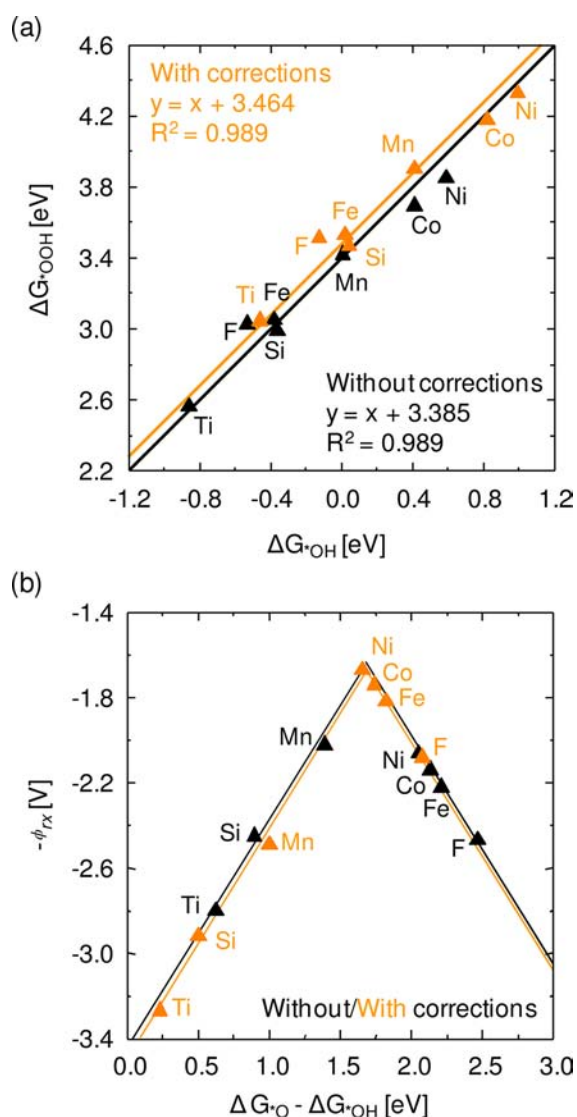

Figure 6. (a) Binding energies of *OOH versus binding energies of *OH for the pure and doped fully hydroxylated (1×1) Fe_2O_3 (0001) surfaces under vacuum, with different $U - J$ values for different dopants. The linear fit is constrained to have a slope of 1. (b) The negative of the reaction potentials ($-\phi_{rx}$) versus the binding energy differences of $\Delta G_{*O} - \Delta G_{*OH}$. The orange (black) curve represents the results with (without) ZPE and entropic corrections.

from eqs 3, 4, and 6−8. According to this scaling relationship, the closer $\Delta G_{*O} - \Delta G_{*OH}$ is with respect to $3.464/2 = 1.732$ eV, the smaller the reaction potential, ϕ_{rx}. This is confirmed by the plot of $-\phi_{rx}$ versus $\Delta G_{*O} - \Delta G_{*OH}$ in Figure 6b. Practically at the peak of the orange volcano curve[84] is the case for Ni doping, located near $\Delta G_{*O} - \Delta G_{*OH} = 1.7$ eV. The maximum expected activity is predicted because Ni doping provides the optimal relative binding strengths of *OH and *OOH. Including ZPE and entropic corrections adds different constants to the values of ΔG_{*O}, ΔG_{*OH}, and ΔG_{*OOH} (see Table 2). Comparing the black and orange curves in Figure 6, these corrections shift both the peak positions of the volcano curves and the relative positions of dopants on the curves. These corrections make a qualitative difference in our predictions; in general, ZPE and entropic corrections to quantum mechanical energies at 0 K should always be added to model experimental conditions at finite temperature. In the literature these corrections are usually accounted for,[53,54,61,85] but they are sometimes omitted when several varieties of oxide surfaces are under investigation.[55] Based on the orange volcano curve in Figure 6b, since the ϕ_{rx} for pure hematite lies close to the peak position of the volcano curve, only modest improvement can be expected over pure hematite.

To further understand why different dopants affect $\Delta G_{*O} - \Delta G_{*OH}$ values, we analyze various properties of the reactive species. In Figure 7, $\Delta G_{*O} - \Delta G_{*OH}$ is plotted against each specific dopant (or "Fe" in the case of pure hematite). It is clear that the $\Delta G_{*O} - \Delta G_{*OH}$ values are inversely related to the Bader charges of the transition metals and the VBM of the doped slabs, that is, the larger the Bader charges of the transition metal cations (or the higher the VBM of the doped slabs), the smaller the $\Delta G_{*O} - \Delta G_{*OH}$. The VBM values are less negative when more positively charged dopants are near the surface because such dopants draw out electrons from the bulk material making it easier to remove an electron from the surface. The VBM for the F-doped slab is the most negative because the F atom is negatively charged and suppresses electrons coming from the bulk. In contrast, $\Delta G_{*O} - \Delta G_{*OH}$ values correlate well with the Bader charges of the circled O anions in *O and *OOH (Figure 3). These are more positive than the normal Bader charges of O, indicating probable hole localization on these O anions. Hole localization on O makes sense during the water oxidation reaction, where the oxidation states of O change from −2 to 0. Dopants that are more positively charged than Fe favor formation of *O on the surface (reaction C) because they help stabilize a more negatively charged O anion formed upon deprotonation. However, that more negatively charged O anion makes *OOH formation (reaction D) unfavorable, consistent with the relation that shows the trade-off between reactions C and D: $\Delta G_{*OOH} - \Delta G_{*OH} = (\Delta G_{*OOH} - \Delta G_{*O}) + (\Delta G_{*O} - \Delta G_{*OH}) = \Delta G_D + \Delta G_C = 3.464$ (see equation within Figure 6a and eq 10). On the other hand, when the dopants are less positively charged than Fe, the O anions are less negatively charged. This favors *OOH formation but not *O formation. Therefore, we conclude that the most energetically favorable pathway requires moderate propensity for hole localization on the active O anions. The balanced bonding from Ni doping therefore gives the smallest reaction potential.

4.4. Perspectives on Photoelectrocatalysis and Our Model. Developing efficient photoelectrocatalysts requires optimizing various properties (e.g., band gaps, band edge character and alignments, electron/hole conductivity and
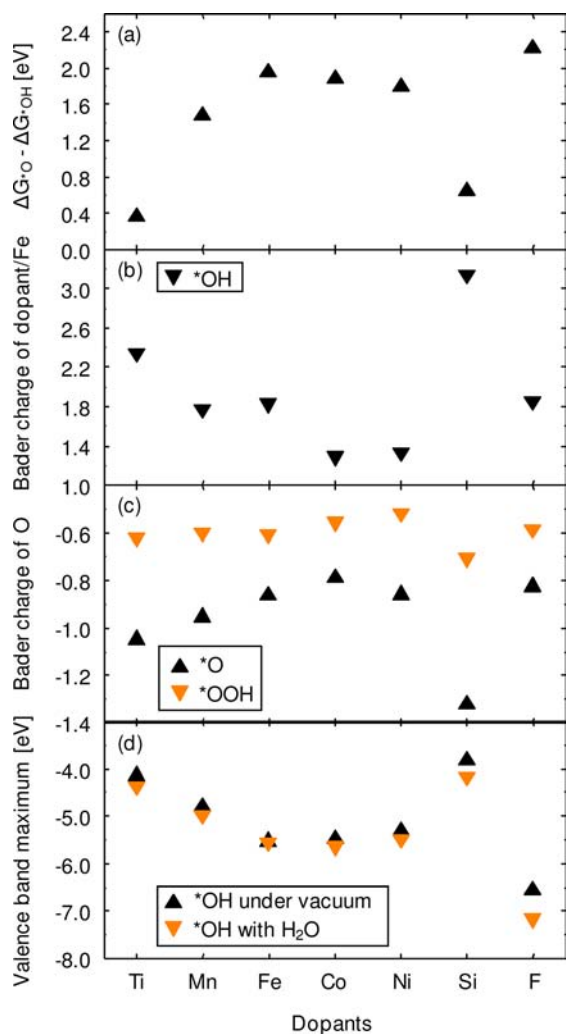
Figure 7. Various properties of the intermediate species in the water oxidation reaction on the pure ("Fe") and doped fully hydroxylated (1×1) Fe_2O_3 (0001) surfaces under vacuum or in solvent, using different $U - J$ values for different first-row transition metal dopants. (a) $\Delta G_{*O} - \Delta G_{*OH}$ for slabs with different dopants. (b) Bader charges of Ti, Mn, Co, Ni, and Si dopants and Fe at the same cation substitution site for pure and F-doped surfaces. (c) Average Bader charges for *O and *OOH for the O anions in orange circles in Figure 2. (d) The valence band maximum for each slab with different dopants, under vacuum or in solvent.

lifetime, and reaction thermodynamics and kinetics). The current study focuses on reaction thermodynamics only. Water oxidation reaction steps are simulated here at the periodic DFT +U level by referencing to the SHE to avoid explicit modeling of proton release into water and electron injection into the semiconductor. Referencing to the SHE greatly simplifies the computation and has been successfully demonstrated in previous electrochemical modeling.[53−55,61,81,85] The model we adopt also does not account for photoexcited holes within hematite. However, Valdéz and Kroes reported a DFT study on TiO_2 showing that calculations using neutral clusters as reactive catalysts give very similar results as calculations on positively charged clusters with one hole.[86] They also showed that these cluster calculations gave similar results as periodic DFT calculations. Physically, localized holes at the hematite surface should enhance water oxidation, thus charge neutral models should provide a theoretical upper bound for overpotential

estimates based on thermodynamics. On the other hand, since kinetic barriers were not evaluated here, the estimated overpotentials based on thermodynamics are lower bound estimates for the measured overpotentials. These two counter factors compete, resulting in error cancellation to some degree. Experimentally, the overpotential for the hematite photoanode has most recently been estimated at 0.5−0.6 V.[5] Our calculated overpotential of 0.77 V for liquid-phase reaction on a pure (1×1) hematite slab (denoting 1/3 ML reactive sites) is just slightly above that experimental range, showing this model's approximate predictive capacity. Lower reactive site (and dopant) coverages give slightly higher overpotentials, but these may be less representative of a typical hematite/water interface that likely contains significant concentrations of defects (vacancies, grain boundaries, etc.) that will promote reactive site formation. Of course, the ultimate comparison with experiment awaits evaluation of kinetic barriers to confirm or exclude the model's validity.

Photoelectrocatalytic water oxidation on hematite starts with light absorption in the near surface region of hematite. The resulting electrons and holes in the hematite anode are then separated: electrons flow to the external circuit, while holes migrate to the surface and react with water. Previously, theoretical calculations on optical excitations of pure hematite using an electrostatically embedded cluster showed that a charge transfer excitation from O to Fe is much higher in energy than the Fe $d−d$ transition.[87] Since hole localization on O is necessary in the water oxidation reaction (O evolves from −2 to 0 charge), the unfavorable ligand-to-metal charge transfer (LMCT) may limit the hole concentration on O in undoped hematite photoanodes, which in turn reduces their efficiencies.

Doping can enhance the efficiency of photoelectrocatalysis on hematite through different means. In the light absorption process, introducing other cation elements with lower-lying LMCT excitation states in their oxide phases might increase photogenerated hole concentrations on O anions. Since mid-to-late first-row transition metal oxides are of mixed Mott−Hubbard and charge-transfer character,[88] doping hematite with Co or Ni might promote O hole concentration via LMCT between Co/Ni and O centers. Moreover, surface modifications with different dopants will affect the VBM level of the hematite slabs. Specifically, Ti, Mn, or Si doping shifts the VBM to be less negative, while F doping shifts the VBM to be more negative (Figure 7d). The VBM for Co- or Ni-doped slabs are largely unaffected by doping. Since the CBM position of hematite is below that needed for water reduction, it is desirable to shift the VBM and CBM of hematite to less negative values. Therefore, surface modifications with Ti, Mn, or Si should lead to favorable VBM alignments while the CBM alignment needs to be further verified by characterizing band gap changes after the modifications. In terms of electron transport in doped hematite, our earlier theoretical work on electron transport suggested that Si is a more favorable dopant than Ti in the low doping concentration limit.[10] Therefore, we suggest that Si is a better dopant than Ti to improve band alignment and electron transport in hematite photoanodes. On the other hand, we predict that Ti or Si doping increases the water oxidation overpotential on hematite surfaces, with Ti doping giving the highest ϕ_{rx}.

Lastly, we have shown that dopants adjacent to reaction sites change reaction thermodynamics. The presence of dopants can modulate the bonding strengths between the surface and the intermediate adsorbed species in the water oxidation reaction.

According to the Sabatier principle, interactions between the catalysts and the adsorbates should be intermediate: neither too weak to adsorb the reactants nor too strong as to inhibit product leaving the catalyst. Among a series of dopants, Co and Ni are predicted as the most effective additives to reduce overpotentials because their less positive charge compared to Fe provides optimal binding strengths to the O, OH, and OOH adsorbates. Indeed, after submission of this work, we discovered recently published measurements of photoelectrochemical properties of Ni-doped hematite by Liu et al.[21] That study reported that Ni-doping leads to higher photocurrent densities for water oxidation compared to pure hematite samples. The improved performance of the Ni-doped hematite surface was attributed to increased conductivity and higher charge separation efficiency, but our work suggests additionally that the reaction thermodynamics is improved. An observed reduction of 0.05 V in the onset potential for Ni-doped samples further validates our predictions for the effectiveness of Ni-doped hematite.

5. CONCLUSIONS

We performed *ab initio* DFT+U calculations to characterize the thermodynamics of water oxidation on the hematite (0001) surface. Our previous work[72] demonstrated that extensions beyond standard DFT (i.e., *ab initio* DFT+U) must be employed to obtain accurate structures and electronic properties of hematite. In the present work, we calculated reaction potentials for water oxidation in both gas and liquid phases on a (1×1) hydroxylated hematite slab (1/3 ML reactive sites) and in the gas phase for a (2×2) slab (1/12 ML reactive sites). However, since actual hematite electrode surfaces under hydrating conditions undoubtedly have a complex structure with polycrystalline facets, vacancies, and hydroxylation, we expect predictions based on the explicitly solvated, hydroxylated (1×1) slab that contains a higher concentration of reactive sites to be more representative of actual electrochemical conditions. This model gives a reaction potential ϕ_{rx}, defined as the minimum potential that makes $\Delta G \leq 0$ for all individual electrochemical steps, of 1.88 V, corresponding to an overpotential of 0.77 V. This calculated overpotential is in reasonable agreement with measured overpotentials of 0.5−0.6 V for hematite photoanodes.[5]

Cation doping (Ti, Mn, Co, Ni, Si) was introduced by direct cation substitutions, and F doping was introduced by substituting an OH group on the fully hydroxylated surface. Including ZPE and entropic corrections shifts reaction energy levels, qualitatively changing the predictions of which dopants act to reduce the overpotential. By accounting for ZPE and entropic corrections and by using *ab initio* $U - J$ values for the dopants, Co or Ni doping reduces the ϕ_{rx} of pure hematite by up to 0.15 V. In contrast, Ti, Mn, Si, and F doping increased the ϕ_{rx} beyond that of pure hematite, suggesting Co and Ni additions are candidates to improve the catalytic activity of pure hematite. The doping effects were analyzed by comparing charges of the dopants and active O anions as well as the binding energies of O, OH, and OOH adsorbates. Specifically, optimal binding of O, OH, and OOH reactive species is the key to reduce the reaction potential. Co or Ni, both with charges less positive than Fe, produce intermediately charged O anions that best balance the binding strengths among O, OH, and OOH, yielding the smallest reaction potential.

Lastly, after initial submission of this manuscript, we became aware of very recent measurements[21] reporting improved water oxidation activity on Ni-doped hematite photoanodes, which further validates our work. Overall, our results indicate that Ni and Co doping at the hematite surface are best suited to reduce the overpotential for water oxidation on hematite photoanodes.

■ ASSOCIATED CONTENT

ⓢ Supporting Information

Further computational details, unit cell vectors and atomic coordinates, and energies of species discussed in the text. This material is available free of charge via the Internet at http://pubs.acs.org.

■ AUTHOR INFORMATION

Corresponding Author
eac@princeton.edu
Notes
The authors declare no competing financial interest.

■ ACKNOWLEDGMENTS

■ REFERENCES

(1) Bak, T.; Nowotny, J.; Rekas, M.; Sorrell, C. C. *Int. J. Hydrogen Energy* **2002**, *27*, 991.

(2) Merchant, P.; Collins, R.; Kershaw, R.; Dwight, K.; Wold, A. *J. Solid State Chem.* **1979**, *27*, 307.

(3) Glasscock, J. A.; Barnes, P. R. F.; Plumb, I. C.; Bendavid, A.; Martin, P. J. *Thin Solid Films* **2008**, *516*, 1716.

(4) Hu, Y.-S.; Kleiman-Shwarsctein, A.; Stucky, G. D.; McFarland, E. W. *Chem. Commun.* **2009**, 2652.

(5) Sivula, K.; Le Formal, F.; Grätzel, M. *ChemSusChem* **2011**, *4*, 432−449.

(6) Lin, Y.; Yuan, G.; Sheehan, S.; Zhou, S.; Wang, D. *Energy Environ. Sci.* **2011**, *4*, 4862.

(7) Kennedy, J. H.; Anderman, M.; Shinar, R. *J. Electrochem. Soc.* **1981**, *128*, 2371.

(8) Glasscock, J. A.; Barnes, P. R. F.; Plumb, I. C.; Savvides, N. *J. Phys. Chem. C* **2007**, *111*, 16477.

(9) Kumar, P.; Sharma, P.; Shrivastav, R.; Dass, S.; Satsangi, V. R. *Int. J. Hydrogen Energy* **2011**, *36*, 2777.

(10) Liao, P.; Toroker, M. C.; Carter, E. A. *Nano Lett.* **2011**, *11*, 1775.

(11) Cesar, I.; Kay, A.; Gonzalez Martinez, J. A.; Grätzel, M. *J. Am. Chem. Soc.* **2006**, *128*, 4582.

(12) Kay, A.; Cesar, I.; Grätzel, M. *J. Am. Chem. Soc.* **2006**, *128*, 15714.

(13) Cesar, I.; Sivula, K.; Kay, A.; Zboril, R.; Grätzel, M. *J. Phys. Chem. C* **2009**, *113*, 772.

(14) Saremi-Yarahmadi, S.; Wijayantha, K. G. U.; Tahir, A. A.; Vaidhyanathan, B. *J. Phys. Chem. C* **2009**, *113*, 4768.

(15) Souza, F. L.; Lopes, K. P.; Longo, E.; Leite, E. R. *Phys. Chem. Chem. Phys.* **2009**, *11*, 1215.

(16) Zhong, D. K.; Sun, J.; Inumaru, H.; Gamelin, D. R. *J. Am. Chem. Soc.* **2009**, *131*, 6086.

(17) Tilley, S. D.; Cornuz, M.; Sivula, K.; Grätzel, M. *Angew. Chem.* **2010**, *122*, 6549.

(18) Zhong, D. K.; Gamelin, D. R. *J. Am. Chem. Soc.* **2010**, *132*, 4202.

(19) Kleiman-Shwarsctein, A.; Hu, Y.-S.; Forman, A. J.; Stucky, G. D.; McFarland, E. W. *J. Phys. Chem. C* **2008**, *112*, 15900.

(20) Hu, Y.-S.; Kleiman-Shwarsctein, A.; Forman, A. J.; Hazen, D.; Park, J.-N.; McFarland, E. W. *Chem. Mater.* **2008**, *20*, 3803.

(21) Liu, Y.; Yu, Y.-X.; Zhang, W.-D. *Electrochim. Acta* **2012**, *59*, 121.

(22) Finger, L. W.; Hazen, R. M. *J. Appl. Phys.* **1980**, *51*, 5362.

(23) Morin, F. J. *Phys. Rev.* **1950**, *78*, 819.

(24) Lad, R. J.; Henrich, V. E. *Surf. Sci.* **1988**, *193*, 81.

(25) Gautier-Soyer, M.; Pollak, M.; Henriot, M.; Guittet, M. J. *Surf. Sci.* **1996**, *352–354*, 112.

(26) Wang, X. G.; Weiss, W.; Shaikhutdinov, S. K.; Ritter, M.; Petersen, M.; Wagner, F.; Schlogl, R.; Scheffler, M. *Phys. Rev. Lett.* **1998**, *81*, 1038.

(27) Chambers, S. A.; Yi, S. I. *Surf. Sci.* **1999**, *439*, L785.

(28) Shaikhutdinov, S. K.; Weiss, W. *Surf. Sci.* **1999**, *432*, L627.

(29) Thevuthasan, S.; Kim, Y. J.; Yi, S. I.; Chambers, S. A.; Morais, J.; Denecke, R.; Fadley, C. S.; Liu, P.; Kendelewicz, T.; Brown, G. E. *Surf. Sci.* **1999**, *425*, 276.

(30) Henderson, M. A. *Surf. Sci.* **2002**, *515*, 253.

(31) Trainor, T. P.; Chaka, A. M.; Eng, P. J.; Newville, M.; Waychunas, G. A.; Catalano, J. G.; Brown, Jr. *Surf. Sci.* **2004**, *573*, 204.

(32) Tanwar, K. S.; Catalano, J. G.; Petitto, S. C.; Ghose, S. K.; Eng, P. J.; Trainor, T. P. *Surf. Sci.* **2007**, *601*, L59.

(33) Tanwar, K. S.; Lo, C. S.; Eng, P. J.; Catalano, J. G.; Walko, D. A.; Brown, Jr.; Waychunas, G. A.; Chaka, A. M.; Trainor, T. P. *Surf. Sci.* **2007**, *601*, 460.

(34) Yamamoto, S.; Kendelewicz, T.; Newberg, J. T.; Ketteler, G.; Starr, D. E.; Mysak, E. R.; Andersson, K. J.; Ogasawara, H.; Bluhm, H.; Salmeron, M.; Brown, G. E.; Nilsson, A. *J. Phys. Chem. C* **2010**, *114*, 2256.

(35) Liao, P.; Carter, E., A. *J. Mater. Chem.* **2010**, *20*, 6703.

(36) Greene, M. E.; Chiaramonti, A. N.; Christensen, S. T.; Cao, L. X.; Bedzyk, M. J.; Hersam, M. C. *Adv. Mater.* **2005**, *17*, 1765.

(37) Bergermayer, W.; Schweiger, H.; Wimmer, E. *Phys. Rev. B* **2004**, *69*, 195409.

(38) Cohen, A. J.; Mori-Sánchez, P.; Yang, W. *Science* **2008**, *321*, 792.

(39) Sandratskii, L. M.; Uhl, M.; Kübler, J. *J. Phys.: Condensed Matter* **1996**, *8*, 983.

(40) Rollmann, G.; Rohrbach, A.; Entel, P.; Hafner, J. *Phys. Rev. B* **2004**, *69*, 165107.

(41) Anisimov, V. I.; Zaanen, J.; Andersen, O. K. *Phys. Rev. B* **1991**, *44*, 943.

(42) Anisimov, V. I.; Aryasetiawan, F.; Lichtenstein, A. I. *J. Phys.: Condensed Matter* **1997**, *9*, 767.

(43) Hendewerk, M.; Salmeron, M.; Somorjai, G. A. *Surf. Sci.* **1986**, *172*, 544.

(44) Kurtz, R. L.; Henrich, V. E. *Phys. Rev. B* **1987**, *36*, 3413.

(45) Becker, U.; Hochella, M. F.; Apra, E. *Am. Mineral.* **1996**, *81*, 1301.

(46) Junta-Rosso, J. L.; Hochella, M. F., Jr. *Geochim. Cosmochim. Acta* **1996**, *60*, 305.

(47) Liu, P.; Kendelewicz, T.; Brown, G. E.; Nelson, E. J.; Chambers, S. A. *Surf. Sci.* **1998**, *417*, 53.

(48) Eggleston, C. M.; Stack, A. G.; Rosso, K. M.; Higgins, S. R.; Bice, A. M.; Boese, S. W.; Pribyl, R. D.; Nichols, J. J. *Geochim. Cosmochim. Acta* **2003**, *67*, 985.

(49) Parker, S. C.; de Leeuw, N. H.; Redfern, S. E. *Faraday Discuss.* **1999**, *114*, 381.

(50) Jones, F.; Rohl, A. L.; Farrow, J. B.; van Bronswijk, W. *Phys. Chem. Chem. Phys.* **2000**, *2*, 3209.

(51) Yin, S.; Ma, X.; Ellis, D. *Surf. Sci.* **2007**, *601*, 2426.

(52) Yin, S.; Ellis, D. E. *Surf. Sci.* **2008**, *602*, 2047.

(53) Rossmeisl, J.; Qu, Z. W.; Zhu, H.; Kroes, G. J.; Nørskov, J. K. *J. Electroanal. Chem.* **2007**, *607*, 83.

(54) Valdés, Á.; Qu, Z. W.; Kroes, G. J.; Rossmeisl, J.; Nørskov, J. K. *J. Phys. Chem. C* **2008**, *112*, 9872.

(55) Man, I. C.; Su, H.-Y.; Calle-Vallejo, F.; Hansen, H. A.; Martínez, J. I.; Inoglu, N. G.; Kitchin, J.; Jaramillo, T. F.; Nørskov, J. K.; Rossmeisl, J. *ChemCatChem* **2011**, *3*, 1159.

(56) Filhol, J.-S.; Neurock, M. *Angew. Chem., Int. Ed.* **2006**, *45*, 402.

(57) Rossmeisl, J.; Nørskov, J. K.; Taylor, C. D.; Janik, M. J.; Neurock, M. *J. Phys. Chem. B* **2006**, *110*, 21833.

(58) Taylor, C. D.; Wasileski, S. A.; Filhol, J.-S.; Neurock, M. *Phys. Rev. B* **2006**, *73*, 165402.

(59) Rossmeisl, J.; Skúlason, E.; Björketun, M. E.; Tripkovic, V.; Nørskov, J. K. *Chem. Phys. Lett.* **2008**, *466*, 68.

(60) Janik, M. J.; Taylor, C. D.; Neurock, M. *J. Electrochem. Soc.* **2009**, *156*, B126.

(61) Rossmeisl, J.; Logadottir, A.; Nørskov, J. K. *Chem. Phys.* **2005**, *319*, 178.

(62) Kresse, G.; Hafner, J. *Phys. Rev. B* **1993**, *47*, 558.

(63) Kresse, G.; Furthmüller, J. *Comput. Mater. Sci.* **1996**, *6*, 15.

(64) Perdew, J. P.; Burke, K.; Ernzerhof, M. *Phys. Rev. Lett.* **1996**, *77*, 3865.

(65) Blöchl, P. E. *Phys. Rev. B* **1994**, *50*, 17953.

(66) Kresse, G.; Joubert, D. *Phys. Rev. B* **1999**, *59*, 1758.

(67) Zhou, F.; Cococcioni, M.; Marianetti, C. A.; Morgan, D.; Ceder, G. *Phys. Rev. B* **2004**, *70*, 235121.

(68) Wang, L.; Maxisch, T.; Ceder, G. *Phys. Rev. B* **2006**, *73*, 195107.

(69) Dudarev, S. L.; Botton, G. A.; Savrasov, S. Y.; Humphreys, C. J.; Sutton, A. P. *Phys. Rev. B* **1998**, *57*, 1505.

(70) Bengone, O.; Alouani, M.; Blochl, P.; Hugel, J. *Phys. Rev. B* **2000**, *62*, 16392.

(71) Mosey, N. J.; Liao, P.; Carter, E. A. *J. Chem. Phys.* **2008**, *129*, 014103.

(72) Liao, P.; Carter, E. A. *Phys. Chem. Chem. Phys.* **2011**, *13*, 15189.

(73) Bocquet, A. E.; Mizokawa, T.; Morikawa, K.; Fujimori, A.; Barman, S. R.; Maiti, K.; Sarma, D. D.; Tokura, Y.; Onoda, M. *Phys. Rev. B* **1996**, *53*, 1161.

(74) Calzado, C. J.; Hernández, N. C.; Sanz, J. F. *Phys. Rev. B* **2008**, *77*, 045118.

(75) Kanan, D. K.; Carter, E. A. *J. Phys. Chem. C* **2012**, *116*, 9876.

(76) Ritzmann, A.; Carter, E. A. In preparation.

(77) Alidoust, N.; Carter, E. A. In preparation.

(78) Zhao, Y.; Truhlar, D. *Theor. Chem. Acc.* **2008**, *120*, 215.

(79) Henkelman, G.; Arnaldsson, A.; Jónsson, H. *Comput. Mater. Sci.* **2006**, *36*, 354.

(80) *CRC Handbook of Chemistry and Physics*, 77th ed.; CRC Press: Boca Raton, FL, 1996–1997.

(81) Keith, J. A.; Jacob, T. *Angew. Chem., Int. Ed.* **2010**, *49*, 9521.

(82) Velev, J.; Bandyopadhyay, A.; Butler, W. H.; Sarker, S. *Phys. Rev. B* **2005**, *71*, 205208.

(83) Fernández, E. M.; Moses, P. G.; Toftelund, A.; Hansen, H. A.; Martínez, J. I.; Abild-Pdersen, F.; Kleis, J.; Hinnemann, B.; Rossmeisl, J.; Bligaard, T.; Nørskov, J. K. *Angew. Chem., Int. Ed.* **2008**, *47*, 4683.

(84) Parsons, R. Volcano Curves in Electrochemistry. In *Catalysis in Electrochemistry: From Fundamental Aspects to Strategies for Fuel Cell Development*; Santos, E., Schmickler, W., Eds.; John Wiley & Sons, Inc.: New York, 2011; pp 1.

(85) Keith, J. A.; Jerkiewicz, G.; Jacob, T. *ChemPhysChem* **2010**, *11*, 2779.

(86) Valdés, A.; Kroes, G.-J. *J. Phys. Chem. C* **2010**, *114*, 1701.

(87) Liao, P.; Carter, E. A. *J. Phys. Chem. C* **2011**, *115*, 20795.

(88) Noguera, C. *Physics and Chemistry at Oxide Surfaces*; Cambridge University Press: New York, 1996.